sensors

MDPI

Article

A Single-Cell Optically Pumped Intrinsic Gradiometer

Nicholaus Zilinski [1], Ash M. Parameswaran [1], Bonnie L. Gray [1] and Teresa Cheung [1,2,*]

[1] School of Engineering Science, Simon Fraser University, Burnaby, BC V5A 1S6, Canada; nzilinsk@sfu.ca (N.Z.); meenakshinathan_parameswaran@sfu.ca (A.M.P.); bonnie_gray@sfu.ca (B.L.G.)
[2] Surrey Memorial Hospital, Fraser Health Authority, Surrey, BC V3V 1Z2, Canada
* Correspondence: tpc5@sfu.ca

Highlights

What are the main findings?

- Demonstrated a single-cell intrinsic optically pumped gradiometer.
- Achieved 267 pT/cm/$\sqrt{\text{Hz}}$ sensitivity and 50 dB common mode rejection ratio.

What are the implications of the main findings?

- Enables simplified biomagnetic sensing.
- Reduces sensor complexity for future OPM systems.

Abstract

Optically pumped magnetometers (OPMs) provide a non-cryogenic alternative to superconducting quantum interference devices (SQUIDs) for detecting weak biomagnetic fields. We report the design, construction, and characterization of a single-cell intrinsic OPM gradiometer. The gradiometer employs a rubidium-87 vapor cell in an orthogonal pump and probe beam configuration. The pump beam was split to illuminate two parallel sensing regions of the cell, separated by a baseline of 3 cm, with opposing circular polarization. A linearly polarized probe beam propagated through both regions and was captured by a balanced polarimeter whose output directly measured the spatial magnetic gradient. This prototype achieved a common-mode rejection ratio exceeding 50 dB and a sensitivity of 267 pT/cm/$\sqrt{\text{Hz}}$ without passive magnetic shielding, using active ambient-field coils. As a proof of concept, we recorded preliminary cardiac-synchronous magnetic measurements using an optical pulse sensor for beat segmentation. After bandpass filtering and ensemble averaging, a cardiac-synchronous waveform was observed, consistent with cardiac timing. Unlike many multi-cell gradiometers that require complex calibration, modulation, and passive shielding, this single-cell design reduces cost and complexity.

Keywords: optically pumped magnetometer; intrinsic gradiometer; biomagnetic sensing; common-mode rejection

Academic Editor: Galina V. Kurlyandskaya

Received: 21 January 2026
Revised: 3 March 2026
Accepted: 4 March 2026
Published: 6 March 2026

1. Introduction

Non-invasive imaging is a crucial aspect of modern clinical diagnostics, enabling visualization of internal physiology without the need for surgery [1]. Among these techniques, functional brain and heart imaging provide insight into the electromagnetic activity underlying physiological processes [2]. While magnetic resonance imaging (MRI) reveals anatomical structure, magnetoencephalography (MEG) and magnetocardiography (MCG) provide insight into underlying electromagnetic processes [3,4]. MEG and MCG detect the

tiny magnetic fields generated by neuronal ionic currents and cardiac electrophysiology. By measuring and mapping these fields, MEG and MCG provide direct, non-invasive insight into physiological dynamics, aiding the diagnosis of neurological disorders and cardiac conditions. Until recently, MEG systems have relied on superconducting quantum interference devices (SQUIDs) to achieve the sensitivity required to detect biomagnetic fields [5]. However, these sensors require cryogenic cooling with liquid helium, resulting in bulky, immobile setups that typically use magnetically shielded rooms and ongoing maintenance. These practical limitations contribute to high costs and, consequently, have hindered the widespread use of biomagnetic sensing beyond research [6]. Recent advances in physics and engineering, such as the development of stable, narrow-linewidth lasers, have enabled optically pumped magnetometers (OPMs) to rival the sensitivity offered by SQUIDs [7,8]. OPMs can operate near room temperature and can form flexible systems, allowing sensors to be placed directly on the scalp. This significantly increases signal amplitude, enabling the construction of flexible systems that accommodate diverse head anatomies, including pediatric applications. Several groups have demonstrated the advantages of OPM-based MEG systems, showing improved signal-to-noise ratio, higher resolution, and lower cost [9–11]. Similarly, OPM-based MCG has shown promise for cardiac diagnostics, including arrhythmia detection and fetal monitoring, where non-invasive magnetic sensing offers unique advantages over electrocardiography [12,13].

OPMs can be classified into several operational categories based on their physics of detection [7,14,15]. Spin-Exchange Relaxation-Free (SERF) OPMs operate near zero field, thereby suppressing spin-exchange relaxation and extending spin coherence times [7,16]. These sensors are highly sensitive but require significant shielding to achieve low ambient fields, making them less practical for clinical applications. Free induction decay sensors measure the transient precession of atomic spins, analogous to nuclear spin precession measurements used in MRI. These sensors offer lower sensitivity than SERF but can operate in environments without passive shielding [14]. There are also Mx and Mz magnetometers that use optical pumping and modulation along different axes to achieve relatively higher sensitivities and bandwidths compared to one another. These sensors can operate in the Earth's field as well, but at the cost of reduced sensitivity and added complexity due to modulation. OPM modulation schemes typically require additional electronics, precise calibration and timing, increasing sensor complexity and cost. Eliminating modulation simplifies the optical and electronic design, improving the manufacturability of sensors and arrays. Many sensors do not fit neatly into any one of these categories, and designs often blend features to achieve desired characteristics.

Magnetometers in these categories measure the absolute field at a single point, typically expressed in Tesla (T). In contrast, gradiometers measure the spatial difference in magnetic field strength between two points, typically expressed in Tesla per meter (T/m). These configurations, known as gradiometers, are critical for biomagnetic sensing in noisy environments. They passively reject common-mode magnetic noise, enhancing SNR.

Unlike previous gradiometer designs that rely on multiple lasers, multiple vapor cells, shielding, or complex modulation schemes, the approach presented here uses a single cell with shared pump and probe beams, active field compensation coils, no modulation, and no passive shielding. This eliminates cross-sensor calibration between lasers and cells, reduces cost, and improves manufacturability.

In an intrinsic, single-cell configuration, two spatially separated pump regions are integrated by a shared probe beam. Each region acts as an independent magnetometer, and by applying pump beams of opposing helicity, they produce an equal and opposite response to common-mode magnetic fields. The resultant output of this configuration is a response to the spatial magnetic gradient, a differential measurement between the two regions. This

architecture ensures that both sensing volumes have well-matched conditions, including temperature and vapor density. Such a design enhances common-mode noise rejection, improves sensing volume matching, and avoids additive noise growth by sharing a common sensing volume. However, most intrinsic gradiometer designs require shielding (both active and passive) or complex modulation to operate, limiting their practical real-world use. To date, few demonstrations have shown intrinsic gradiometers operating successfully in an environment without passive shielding or detecting biomagnetic signals [17–20].

This work presents the design, construction, and characterization of a single-cell, optically pumped intrinsic gradiometer operating in a laboratory environment using active field compensation and without passive shielding. The sensor was developed to validate whether a simplified intrinsic gradiometer design could demonstrate sufficient common-mode rejection while maintaining a sensitivity capable of detecting biomagnetic signals. The contributions of this work are: (1) a simplified architecture for the construction of optically single-cell intrinsic gradiometers, (2) characterization of sensitivity, bandwidth, and common-mode rejection, and (3) a proof-of-concept cardiac-synchronous magnetic measurement.

2. Materials and Methods

2.1. Sensor Overview

The optically pumped intrinsic gradiometer presented in this work was designed for operation without passive magnetic shielding, using active compensation coils, and validated in a laboratory setting at Simon Fraser University in Burnaby, Canada. It consists of a single Rb^{87} vapor cell (GC19075-RB, Thorlabs, Newton, NJ, USA) divided into two sensing volumes, illuminated by a set of pump and probe beams. Each sensing volume operates as a single-axis vector magnetometer, measuring the magnetic field orthogonal to the pump and probe beam axes. The intrinsic gradiometer therefore measures the spatial gradient of these field components along the sensor baseline. The goal of this architecture was to demonstrate a simplified, off-the-shelf design that could successfully operate in such environments [21]. A schematic of the sensor geometry is shown in Figure 1.

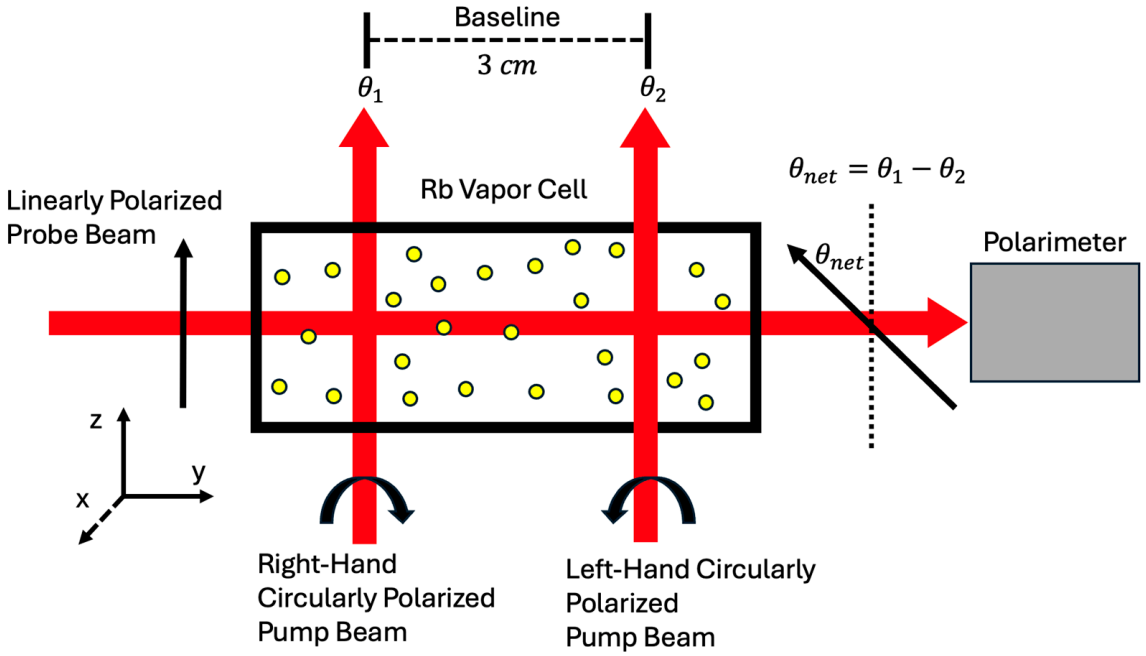

Figure 1. Geometry of a Rb^{87} single-cell optically pumped intrinsic gradiometer. Two pump beams of opposing circular helicity optically pump two spatially separated volumes in the cell. The linearly polarized probe beam traverses both active volumes, undergoing a Faraday rotation θ_1 in the first

volume and θ_2 in the second volume. The gradiometric output produces a differential rotation, $\theta_{net} = \theta_1 - \theta_2$, proportional to the difference in magnetic field between the two volumes. The first volume is sensitive to fields along the +x axis, and the second volume along −x. The amount of rotation is measured by a balanced polarimeter that captures the probe beam as it exits the cell. Red arrows indicate beam propagation direction, black arrows indicate polarization direction. The dashed line represents the probe beam polarization direction before passing through the cell.

2.2. The Atomic Vapor

The sensing medium was an enhanced rubidium-87 vapor cell (d = 25.4 mm, l = 71.8 mm), where d is the diameter of the cell and l is the length. The cell contains 100 Torr of nitrogen buffer gas and was heated to 120 °C using an HTK1000 (Thorlabs, Newton, NJ, USA) resistive heater powered by a standard laboratory power supply (KI 1353B, King Instrument Electronics, legacy laboratory). The cell used no coatings, and the sensing volumes were defined by two oppositely polarized pump beams of opposing circular polarizations.

2.3. Optical System

Two 795 nm, 40 mW distributed Bragg reflector (DBR) diode lasers (Thorlabs, Newton, NJ, USA) were used for the pump and probe beams and tuned near the D1 line of Rb^{87}. Both lasers are DBR795PN laser diodes purchased from Thorlabs along with two CLD1015 laser drivers (Thorlabs, Newton, NJ, USA). These lasers and drivers were chosen for their narrow linewidth, tunability, and stability. The pump beam was expanded to a diameter of 1 cm and divided into two beams using a 50:50 beam splitter. The first beam was left-hand circularly polarized and illuminated a sensing volume in the first half of the cell. The second beam was right-hand circularly polarized and illuminated a sensing volume in the second half of the cell. The probe beam was aligned to propagate orthogonally to the two parallel pump beams, expanded to a diameter of 5 mm, and linearly polarized. A balanced polarimeter captured the probe beam once it had traversed the vapor cell, measuring optical rotation. The sensor schematic is shown in Figure 2.

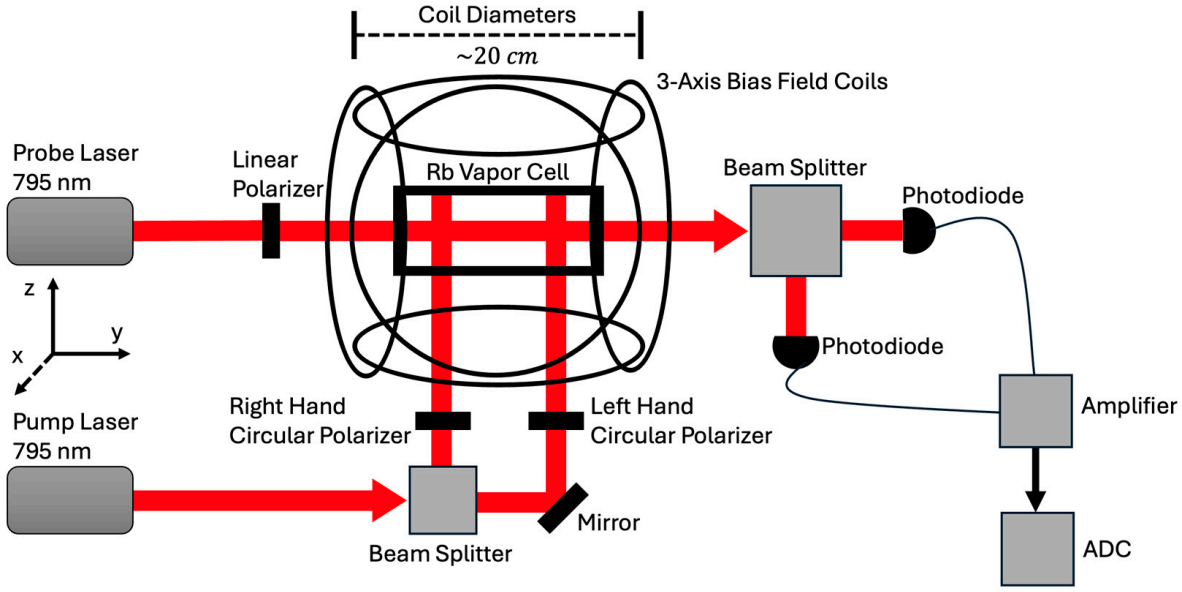

Figure 2. Optical layout and readout of the Rb^{87} intrinsic gradiometer. A 795 nm probe beam is linearly polarized and passes through the vapor cell, while a 795 nm pump beam is split into two equal

beams, propagating orthogonally to the probe beam, and circularly polarized with opposing helicity to define two spatially separated sensing volumes. Passing through the cell, the probe beam will have rotated its polarization in proportion to the difference in ambient field between the volumes. A balanced polarimeter measures the rotation by passing vertical and horizontal polarization components to photodiodes. The components are passed to a transimpedance amplifier and finally digitized by an ADC. Red arrows indicated beam propagation direction, the black arrow indicates an electrical connection between components. Grey and black shapes represent electronic and optical components of the sensor.

2.4. Magnetic Field Control

Three orthogonal sets of Helmholtz coils were used to null the ambient field and apply a bias field at the sensor location. The coil pairs were oriented to produce controllable magnetic fields along each of the sensor axes, as shown in Figure 2. The Helmholtz coils were constructed by winding six 100-turn loops of magnet wire with a diameter of approximately 20 cm. The loops were joined into pairs and mounted into a cube formation. The coils were powered by three separate channels on a standard benchtop power supply (KI 1353B, King Instrument Electronics Co., Garden Grove, CA, USA, legacy laboratory equipement). Using the three axis magnetometer of an iPhone 14 Pro Max (Apple Inc., Cupertino, CA, USA), it was confirmed that the coils reduced the ambient field from ~60 μT to ~500 nT. Typical currents used to null the field were approximately $I_x \approx 75$ mA, $I_y \approx 20$ mA, $I_z \approx 20$ mA (values depend on sensor location and time), where I_x is the current producing the magnetic field along the x-axis, I_y is the current producing the magnetic field along the y-axis, and I_z is the current producing the field along the z-axis.

The vapor cell was heated using an electrically driven heater integrated with the cell. The heater current associated with the wiring introduced a local magnetic field within the cell that could not be measured by external field probes. As a result, the effective field experienced by the atomic ensembles could not be determined precisely. In practice, the operating bias field was set empirically by adjusting the coil currents to maximize the signal response to an applied calibration test tone. The maximum output signal amplitude defined the optimal operating point of the sensor.

Two phantom coils were constructed. The first was a small (d ≈ 1 cm) 20-turn loop of magnet wire to apply differential fields. The second was a large (d ≈ 30 cm) 20-turn loop of magnet wire to apply common-mode fields. These coils provide a controllable field source and are used to generate test fields for calibration and validation. The coils were driven by a standard benchtop function generator (PM 5132, Philips, Eindhoven, The Netherlands), applying a sinusoidal voltage to the loop in series with a 100 Ω resistor.

A the three axis magnetometer was used to calibrate a conversion factor between voltage and magnetic field strength for each phantom. By placing the small phantom centered above one sensing region, a known magnetic field was applied directly to each region independently. The common-mode field was produced by placing both sensing regions in the plane of the large phantom. A known differential field was created by translating the large loop away from the sensor, such that the distance between the sensor and the loop edge was 30 cm.

We defined the effective gradient along the baseline as $\nabla B \approx \Delta B/\Delta y$, where $\Delta B = B_1 - B_2$ is the difference in magnetic field strength between the center of the first and second sensing regions, and $\Delta y = 3$ cm is the center-to-center baseline separation. The baseline was set primarily by the vapor cell geometry and the optical access required for the pump beams. In total, 3 cm was the maximum baseline achievable in this current sensor configuration.

2.5. Electronics and Signal Acquisition

Photodiode signals from each channel of the balanced polarimeter were amplified using low-noise transimpedance amplifiers (AMP110, Thorlabs, Newton, NJ, USA)) with a gain of 10^6 V/A. The amplifiers had a bandwidth of 1 kHz, and the signals were digitized by a Rigol DS1054Z oscilloscope (Rigol Technologies, Suzhou, China). The bandwidth of the amplifiers constrained the sensor bandwidth, as shown in Figure 3. The signal response grew slightly, ~1 dB, from 1 to 100 Hz and rolled off as expected, approaching 1 kHz and beyond.

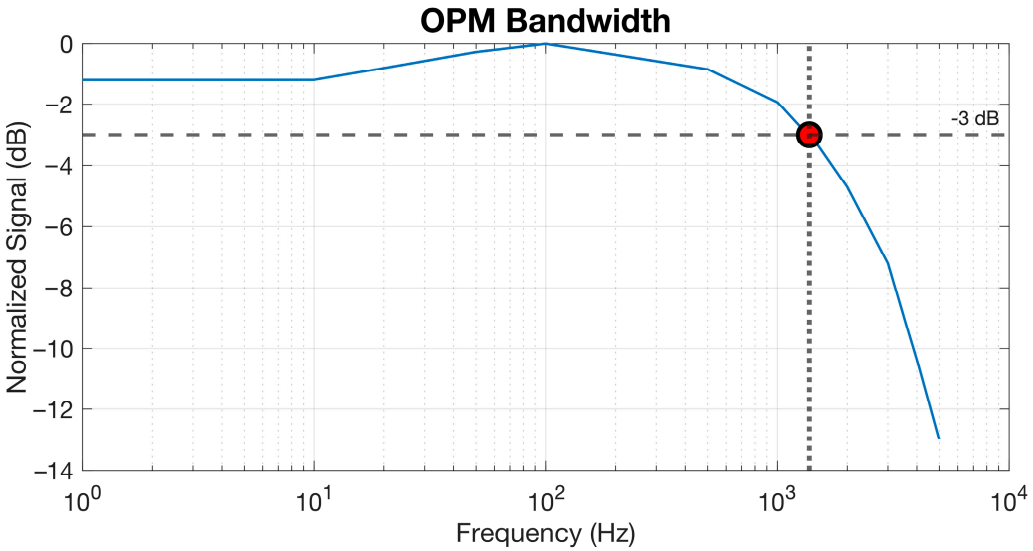

Figure 3. Measured frequency response of the sensor output under a swept sinusoidal calibration field. The amplitude is normalized and shown in dB. The −3 dB cutoff occurs at approximately 1372 Hz, consistent with the electronics-limited bandwidth of the transimpedance amplifier. The blue curve shows the normalized frequency response. The dashed line indicates the amplitude and frequency corresponding to the −3 dB cutoff and the red marker indicates the −3 dB point.

The sensor bandwidth was characterized by applying a swept sinusoidal calibration field to the small phantom coil and measuring the sensor output amplitude as a function of frequency. The response was normalized, and the −3 dB point was taken as the sensor bandwidth. The measured −3 dB cutoff occurred at approximately 1372 Hz, consistent with the electronics-limited bandwidth of the transimpedance amplifiers.

Calibration data were collected at 2.5 MSa/s with 1.2 s record length per capture. Cardiac data were collected at 12.5 kSa/s with 20 s record length per capture. No modulation or lock-in techniques were used in this sensor architecture.

Electrical power consumption, including laser drivers, Helmholtz coils, vapor cell heater, and associated electronics, was not measured or optimized for this prototype. The present work focuses on the proof-of-concept sensor architecture and operation. Power and form-factor are important considerations for scalability and are left for future work.

2.6. Calibration and Characterization

Calibration was performed by applying a known magnetic field to each sensing volume individually. By covering one of the pump beams, only one region is illuminated at a time, functionally transforming the gradiometer into a magnetometer. With the cell heated and lasers on, the first step is to tune the pump beams by sweeping the wavelength across the D_1 transition. Since the sensing regions share a cell, tuning the pump beam only needs to be performed once. When the pump beam was tuned to the vapor's resonance, the signal output amplitude reached a maximum. The same procedure was followed for the probe beam, but the maximum response is found slightly off resonance. This achieves

strong optical interaction while avoiding excessive probe-induced perturbation of the atomic polarization.

With both the pump and probe beams calibrated, the Helmholtz coils were used to null the ambient DC magnetic field and apply a bias field. A similar sweeping technique was performed for each coil axis iteratively until the maximum signal amplitude was achieved. At this stage, the gradiometer was tuned for maximum sensitivity. Helmholtz coils were used to provide a controllable, approximately uniform field over the sensing regions. This reduces field inhomogeneity and supports improved atomic polarization conditions and sensitivity.

The sensitivity of the sensor was characterized by applying a 100 Hz, 300 nT/cm gradient field and analyzing the noise spectrum in the frequency domain via amplitude spectral density. The common-mode rejection ratio (CMRR) was measured by applying a 100 Hz common-mode signal and analyzing the resultant attenuation ratio between the response of the individual sensing regions and the gradient output. A 100 Hz sinusoidal field was used as a benchmark tone for general sensor characterization, as the sensor was developed initially as a more general-purpose gradiometer. This frequency also lies in a relatively low-noise region of the measured spectrum. The following magnetic cardiac measurement is presented as a proof-of-concept biomagnetic demonstration. The reported sensitivity and CMRR values are frequency dependent and should therefore be interpreted under the stated test conditions.

2.7. Magnetic Cardiac Signal

To demonstrate biomagnetic functionality, the first sensing volume was positioned near the chest (~1 cm) to record the magnetic activity produced by the heart. During acquisition, the Helmholtz coils remained in place to maintain ambient field nulling and the applied bias field. To enable close sensor-to-chest spacing, the sensing region was positioned near the edge of the coil volume. Field nulling, sensor tuning, and calibration were maintained, and this geometry was a practical compromise for the proof-of-concept setup. Eleven 20 s trials were performed, and the data were collected and digitized by the Rigol 1054Z oscilloscope. Because the magnetic cardiac signals were below the noise floor, signal averaging was required to reveal the waveform. To enable averaging, the magnetic traces were time-locked to an optical photoplethysmography (PPG) sensor attached to the finger. This provided precise timing markers corresponding to the pulse peaks. These markers served as triggers for segmenting the magnetic data into individual epochs for subsequent averaging.

2.8. Data Analysis

Noise spectra and cardiac traces were analyzed in the frequency domain by applying the Fourier Transform to the time-domain data. The Fourier Transform decomposes the signal into its constituent frequencies, enabling identification of noise and signal components. Spectral amplitudes were estimated using the pwelch() function in MATLAB R2022a (MathWorks, Natick, MA, USA).

The cardiac traces had a digital bandpass filter of 0.5–40 Hz applied, as this is the typical range for electrocardiogram (ECG) filtering [22]. This range preserves the fundamental cardiac components while attenuating baseline drift and high-frequency noise. The cardiac-synchronous data were collected in parallel with the optical heart rate sensor to time-lock the signals. Each optical pulse peak was labeled in the time domain, and a 800 ms window was applied around each peak (200 ms before, 600 ms after). These windows were used to segment the noisy data into individual beats, enabling ensemble-averaging.

3. Results

3.1. Sensor and Signal Response to Common-Mode Fields

To quantify common mode rejection, a uniform sinusoidal magnetic field ($B_{cm} = B_0 \sin(2\pi f t)$) was applied to both sensing volumes in three measurement configurations. Figure 4 summarizes the three operating modes: single-ended readout of volume 1 (V_1), single-ended readout of volume 2 (V_2), and gradiometer operation where both volumes are pumped, producing the differential output, $V_{diff} = V_1 - V_2$ which suppresses common-mode signals. Figure 4a shows the geometries of each measurement condition, b shows the time domain output of each measurement when B_{cm} is applied, and c shows the amplitude spectral density of each output. Within the spectrum plots, the signal is labeled, along with noise peaks produced by the 60 Hz mains voltage and its harmonics.

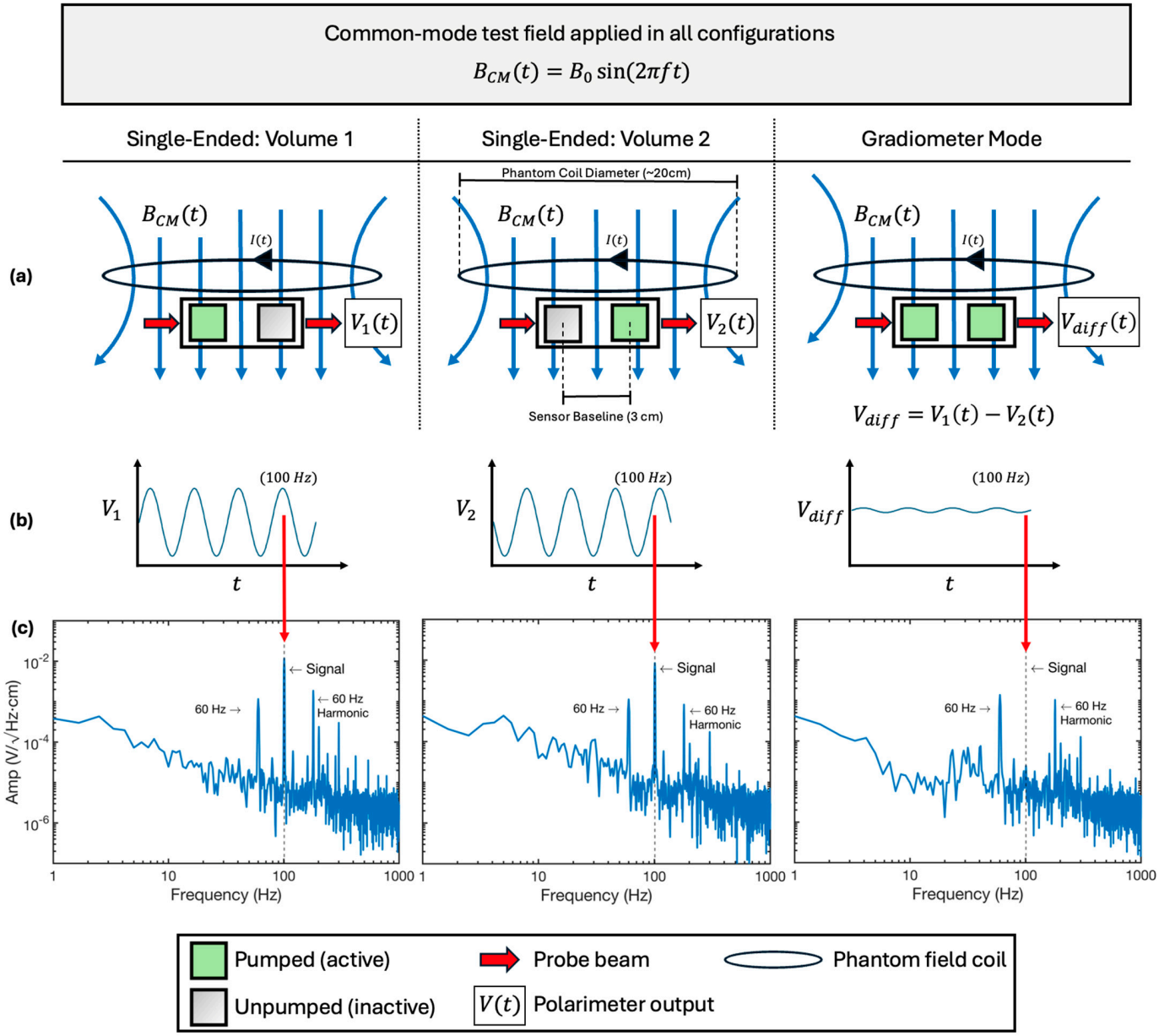

Figure 4. Common-mode measurement configurations and resultant outputs. A uniform, 100 Hz test field, $B_{cm} = B_0 \sin(2\pi f t)$, is applied with a phantom field coil in all cases. The columns show

single-ended operation using sensing volume 1 (V_1), single-ended operation using sensing volume 2 (V_2), and gradiometer mode with differential output $V_{diff} = V_1 - V_2$. (**a**) Schematic configurations of the test conditions, showing which sensing volumes are pumped (active). (**b**) Time-domain representations of the resulting outputs of each configuration. (**c**) Corresponding amplitude spectral densities of the measured outputs, with the signal (dashed line), 60 Hz, and its harmonics labeled.

3.2. Noise Floor and Sensitivity

To quantify the sensor's sensitivity, a known magnetic field gradient was applied across the vapor cell baseline using a phantom coil. The applied gradient was calculated as $\nabla B = \frac{[B(y_1) - B(y_2)]}{\Delta y}$, where $B(y_n)$ is the magnetic field measured by a consumer-grade 3-axis magnetometer at each sensing volume location, and Δy is the baseline of the gradiometer. Figure 5 shows the differential response to the applied 100 Hz gradient field, which was used to calibrate the conversion factor between output voltage and magnetic field gradient. The conversion factor was calculated at 100 Hz as $k = \nabla B_z / A_{100}$, where A_{100} is the magnitude of the 100 Hz spectral peak that was extracted from the amplitude spectral density of the polarimeter output. This calibration enabled the computation of the 267 pT/cm/$\sqrt{\text{Hz}}$ magnetic gradient noise floor, determined by analyzing the median amplitude spectral density over 10–300 Hz. This range was chosen for the median sensitivity estimate because it represents a relatively flat portion of the measured spectrum, excluding the low-frequency rise associated with drift and 1/f environmental noise and high-frequency roll-off from the amplifiers. The 100 Hz test signal is labeled and clearly visible, along with peaks from the 60 Hz mains and its harmonics.

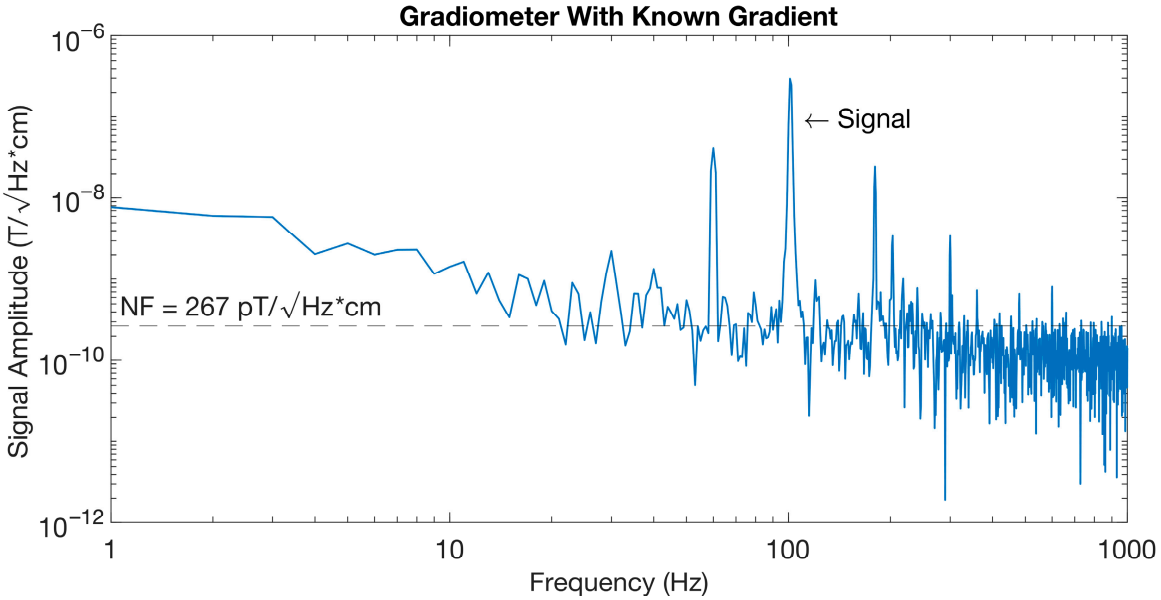

Figure 5. Calibrated amplitude spectral density of the gradiometer output showing the 100 Hz gradient tone and the median noise floor of 267 pT/cm/$\sqrt{\text{Hz}}$ computed over 10–300 Hz.

To identify the dominant contributors to the measured noise floor, the sensor output was recorded under four measurement conditions. This allowed each noise source to be isolated and quantified. Table 1 summarizes which components were active during each condition. The probe condition captured optically related noise by removing the vapor cell from the sensor and disabling the phantom driver. The electronic condition was obtained by unplugging the photodiodes, isolating the front-end electronics as the only signal source in the readout chain. The environmental condition represents the baseline sensor noise in the absence of applied test fields, with the sensor operating normally. The signal condition applied a known test tone using a phantom coil while the sensor

operated normally. Each dataset was converted to an amplitude spectral density using MATLAB's pwelch( ) function (as described earlier). Figure 6 shows these spectra, and that the electronic noise is well below the full system noise across the band, indicating it does not currently limit sensitivity. At low frequency (<10 Hz), the measured spectrum is dominated by 1/f technical/environmental noise. The similarity between probe, signal, and environmental conditions in this band indicates that optical/laser-related noise is a limiting factor for sensitivity. At moderate to high frequencies (50–500 Hz), the probe continues to limit the noise floor, with signal and environmental peaks at the test frequency and 60 Hz and its harmonics. Approaching 1000 Hz, the measured spectrum begins to roll off, consistent with the 1000 Hz bandwidth of the transimpedance amplifier.

Table 1. Noise spectrum collection measurement conditions.

Measurement Condition	Lasers	Phantom	Rb Cell	Amplifiers
Probe	On	Off	Removed	On
Electronic	Off	Off	Not Used	On
Environment	On	Off	Included	On
Signal	On	On	Included	On

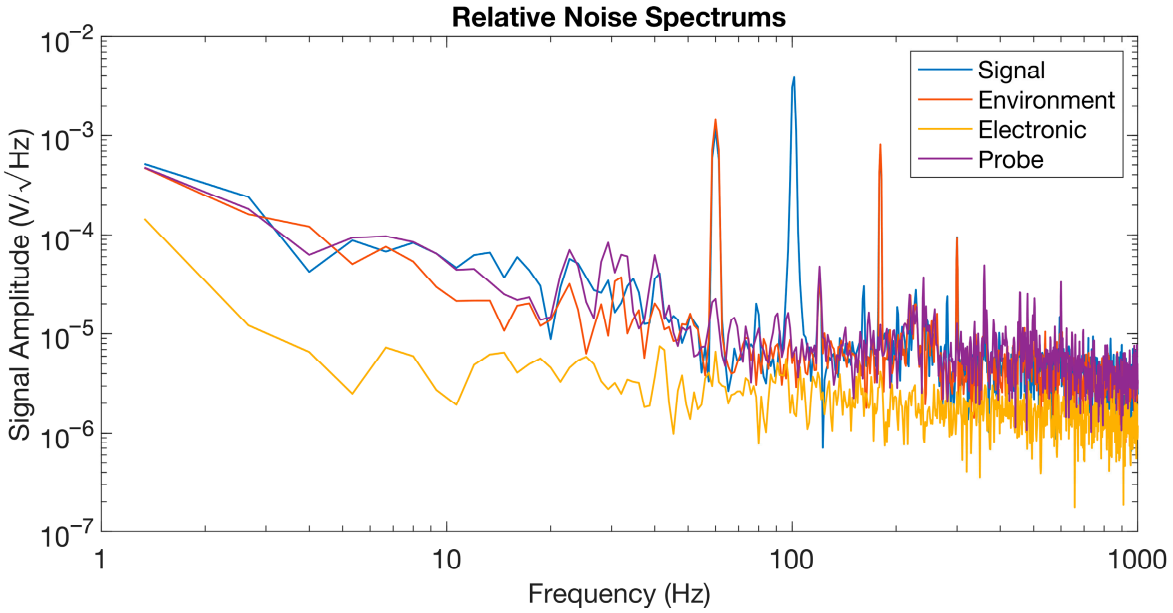

Figure 6. Relative amplitude spectral densities of each noise measurement condition, as outlined in Table 1 (signal, environment, electronic, and probe).

3.3. Cardiac-Synchronous Demonstration

The sensor was positioned approximately 1 cm from the sternum, and 11 trials lasting approximately 20 s were recorded by the researcher. Because individual magnetic epochs were not visually discernible above the noise floor, ensemble averaging was required to reveal the waveform. Signals were time-locked using a custom-built finger photoplethysmography (PPG) sensor, which provided consistent beat-timing references for segmentation. PPG peaks were detected in the filtered PPG trace, and a fixed-length epoch window was defined for each beat. These windows were then mapped onto the magnetic recording as illustrated in Figure 7a. A total of 332 beats were epoched, reducing uncorrelated noise by $\sqrt{332}$.

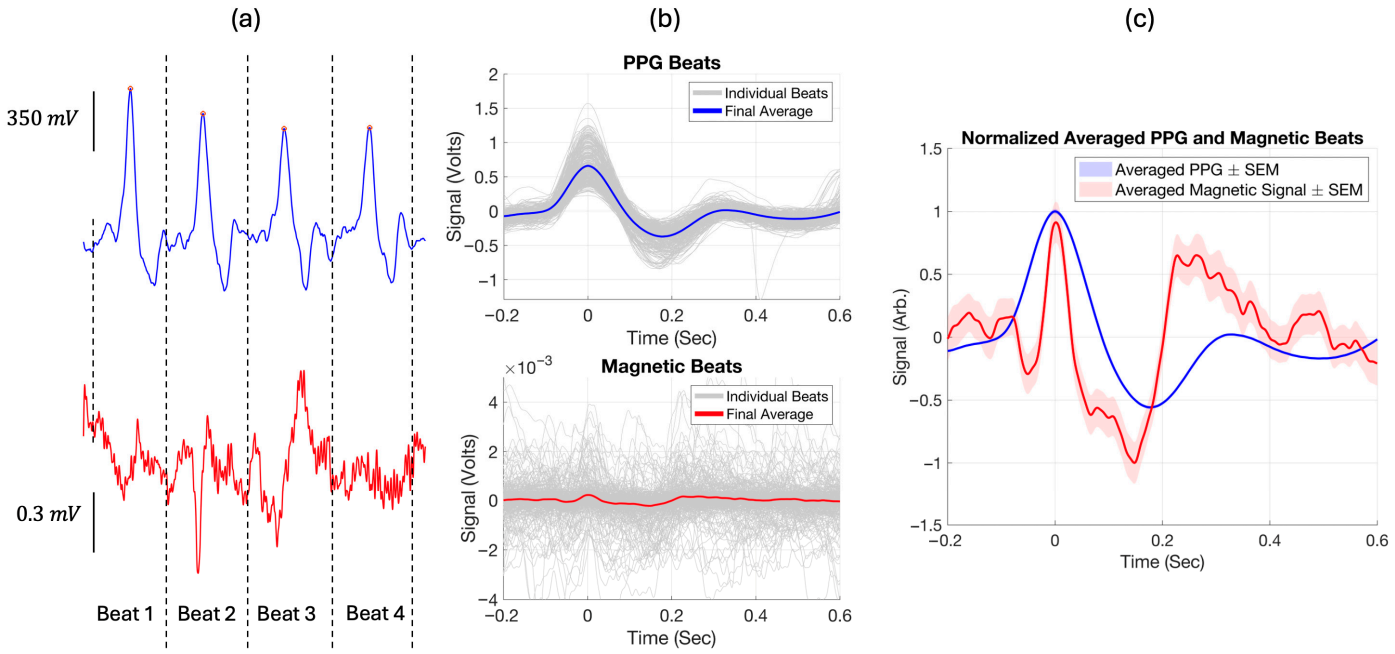

Figure 7. Cardiac time-locking and ensemble averaging used to recover a cardiac-synchronous magnetic waveform. (**a**) Filtered PPG (blue) and simultaneous magnetic (red) traces with beat epoch windows labeled and mapped from the PPG to the magnetic trace. (**b**) Epoched PPG window beats (**top**) and magnetic beats (**bottom**) shown in gray with their corresponding ensemble averages overlaid. (**c**) Comparison of the ensemble-averaged (N = 332) magnetic waveform (red) and ensemble-averaged PPG waveform (blue) aligned such that their peaks occur at t = 0. Shaded regions indicate standard mean error (SEM); the PPG SEM is smaller than the line width at this scale.

After mapping the PPG-derived beat times onto the magnetic recording, fixed-length epochs were extracted and ensemble-averaged over all beats, as shown in Figure 7b. Each epoch was time-aligned such that the PPG peak occurred at t = 0. Figure 7c summarizes the resulting filtered and averaged cardiac-synchronous magnetic signal in comparison to the PPG signal processed in the same pipeline.

3.4. Summary of Key Performance Metrics

The single-cell intrinsic gradiometer operated in a laboratory environment using active field compensation coils, without passive shielding, and enabled the recovery of a cardiac-synchronous waveform. The Table 2 summarizes the key performance metrics reported in this paper.

Table 2. Performance metrics of intrinsic gradiometer.

Metric	Value
Gradient Sensitivity (median ASD 10–300 Hz)	267 pT/cm/$\sqrt{\text{Hz}}$
Bandwidth	1 kHz
CMRR (at 100 Hz)	50 dB

Under the stated test conditions, these results demonstrate that the simplified design achieves competitive bandwidth and CMRR performance using active field compensation, without the need for passive shielding or modulation.

4. Discussion

Despite the advantages offered by OPM-based systems, they continue to face challenges that hinder their adoption as the standard for biomagnetic sensing. This includes

sensor noise, environmental noise rejection, sensor stability, system complexity, and cross-sensor mismatch. Traditional OPM arrays require precise cross-sensor calibration between independent sensors, each of which may drift over time due to changes in temperature and cell integrity [8]. Magnetic gradiometers can be used to mitigate noise by attenuating common-mode fields; however, constructing well-matched sensors with separate cells and electronics can be complex, while also increasing sensor noise levels [23–25]. The measure of how well these common-mode fields are attenuated is known as the common-mode rejection ratio (CMRR). The CMRR is the sensor's ability to suppress common fields relative to its response to differential signals. In this work, the CMRR is computed as $\mathrm{CMRR(dB)} = 20\log\left(\frac{A_{mag}}{A_{grad}}\right)$, where A_{mag} is the amplitude of the output in magnetometer mode and A_{grad} is the amplitude of the output in gradiometer mode. Signal amplitudes are extracted from the frequency spectrum magnitudes. A high CMRR is essential for rejecting environmental noise, and typical values for OPM-based gradiometers using shielding or modulation range from 40 to 60 dB [18–20]. Achieving 50 dB using active field compensation, without passive shielding or modulation, places this design within the competitive range while significantly reducing complexity.

In 2020, Zhang et al. [18] presented a cesium-based intrinsic gradiometer capable of recording a magnetocardiogram (MCG) in an unshielded environment. This sensor achieved a sensitivity of 18 $\mathrm{fT/cm/\sqrt{Hz}}$ by measuring the polarization of the probe beam, but required modulation of the pump beam, magnetic shielding, and two separate vapor cells. In 2021, V.G. Lucivero et al. [26] demonstrated a rubidium-based magnetic gradiometer using a single vapor cell. This sensor achieved a sensitivity of 10 $\mathrm{fT/cm/\sqrt{Hz}}$ via the precession frequency of the vapor. The sensor required shielding, the probe beam to pass through the cell 60 times, and a precise frequency counter. In 2021, Campbell et al. [19] presented a rubidium-87-based atomic gradiometer based on the optical interference sidebands produced by the vapor cells. The sensor achieved a sensitivity of 25 $\mathrm{fT/cm/\sqrt{Hz}}$ in their unshielded lab environment. This sensor did not require shielding but used two separate vapor cells and required both pump beam modulation and a complex microwave pulse system to form the sidebands. In 2022, Cooper et al. [20] presented a highly sensitive intrinsic radio-frequency gradiometer capable of achieving a sub-fT sensitivity of 0.19 $\mathrm{fT/cm/\sqrt{Hz}}$ and a CMRR of 50 dB. This sensor used two separate cells, required shielding, and functioned only at a single frequency, greatly limiting its biomedical applications. In contrast, the sensor presented here operates with a single vapor cell and without passive shielding or modulation. This approach reduces component count, design complexity, and cost while maintaining practical sensitivity.

The results presented here confirm that the single-cell intrinsic gradiometer operated successfully in a laboratory environment without passive shielding and demonstrated this design's feasibility for practical biomagnetic sensing. In contrast with a magnetometer, which measures the field at a single point, this sensor directly measures the magnetic gradient, enabling passive rejection of common-mode environmental noise. Attenuation of common-mode noise signals is essential for biomagnetic sensing in noisy environments and important for the widespread adoption of MEG and MCG systems. The prototype demonstrated a sensitivity of 267 $\mathrm{pT/cm/\sqrt{Hz}}$ across a bandwidth from 10 to 300 Hz and a CMRR exceeding 50 dB (measured at 100 Hz). These results place this design within the competitive range reported for intrinsic gradiometers, despite its simplified architecture.

These designs represent significant advances in sensitivity but prioritize performance over simplicity. This approach complements these efforts, trading sensitivity for simplicity and bandwidth, focusing on increasing accessibility to MEG and MCG instrumentation. Accordingly, this first tabletop prototype exhibits a higher noise floor than state-of-

the-art OPMs. The value of the approach is that it demonstrates that modulation-free, single-cell intrinsic gradiometry can produce a strong CMRR with sufficient sensitivity for biomagnetics.

We note that the baseline of 3 cm in the current design was constrained by the physical dimensions of the vapor cell. This is shorter than some SQUID gradiometer baselines and benefits from close proximity between the sensor and signal source. Accordingly, the biomagnetic result presented here is intended as a proof of concept rather than an optimized architecture.

Gradiometric detection also introduces a trade-off in sensitivity to deeper sources. Signals originating from deeper sources will produce smaller gradients across the baseline relative to shallow sources and are therefore partially attenuated. This effect is more pronounced for shorter baselines.

The external Helmholtz coils were used for prototyping convenience and are not intended as part of the scalability solution offered by this design. In a practical multi-sensor implementation, each sensor could instead be fitted with compact local compensation coils integrated around the vapor cell. This would mitigate the present large coil form factor and enable a further optimized package.

Future iterations will focus on reducing the dominant environmental and technical noise sources, while retaining a low-complexity design. Because both sensing volumes share a vapor cell, they also share vapor pressure, temperature, buffer pressure, and any impurities. This enables excellent cross-sensor matching, which would otherwise require tedious calibration in multi-cell sensors. Direct measurement of the magnetic field gradient mitigates the increase in additive noise that occurs when using two independent sensors and digitally subtracting them.

As shown in Figure 6, ambient field sources and laser probe noise largely dominate the noise spectrum. Below 10 Hz, the spectrum is dominated by $1/f$ noise; from 10 to 500 Hz, the noise floor is relatively flat with peaks from the 60 Hz mains; and from 500 to 1000 Hz, the noise rolls off with the 1 kHz bandwidth of the transimpedance amplifier. These observations highlight where improvement efforts should be focused to yield the most significant gains. Reducing these noise sources is essential for future work in clinical-grade MCG and MEG performance.

While the MCG demonstration yielded promising results, there are some notable limitations. The measurements were performed on a single subject, and the recorded waveform was ensemble-averaged to recover below the noise floor. The PPG provides beat timing but is not a direct measurement of cardiac electrical activity. Future work will include simultaneous ECG, multiple subjects, and controlled sensor-chest geometry to quantify and further validate the approach presented here.

Despite the relatively high operating noise floor, a cardiac-like waveform was revealed after filtering and averaging. The magnetic waveforms occurred 195 ms before the optical signal, a consistent difference observed between PPG and ECG [27]. The width of the magnetic QRS complex wave is also consistent with the timing reported in the literature [28]. This supports the physiological origin of the detected signal and the sensor's feasibility for practical biomagnetic measurements.

From an engineering perspective, this approach may represent a practical step forward for accessible MEG and MCG instrumentation. However, the current prototype uses a relatively large, off-the-shelf vapor cell which limits the formation of dense arrays due to the cell's footprint. A miniaturized cell combined with smaller optics would allow the sensor to transition from the tabletop to a more practical, small, enclosed package. Microfabricated OPMs have demonstrated that miniaturization is possible without sacrificing performance [25]. Future improvements in laser power, buffer

gas pressure, beam quality, heater stability, and bias field compensation would yield improved sensitivity.

With further improvements like those suggested earlier, the noise floor could approach the low pT/cm/$\sqrt{\text{Hz}}$ range. Overall, these findings demonstrate that practical biomagnetic sensing is feasible with a simplified OPM design, supporting progress toward more accessible MCG and MEG instrumentation.

5. Conclusions

This work demonstrates the feasibility of a simplified, single-cell optically pumped intrinsic gradiometer that can operate in a lab environment using active field compensation coils and without passive shielding. The sensor achieved a noise floor of 267 pT/cm/$\sqrt{\text{Hz}}$, a 1 kHz bandwidth, and a 50 dB CMRR. The 1 kHz bandwidth supports detection of faster transient signals, while the 50 dB CMRR improves attenuation of interference in noisy environments. The 50 dB CMRR is within the competitive range reported for OPM-based intrinsic gradiometers and was accomplished using active field compensation and without modulation or passive shielding. These results verify that intrinsic gradiometry is a viable path forward for biomagnetic sensing. The design's simplicity and use of off-the-shelf components make the sensor highly reproducible. Continued development focusing on noise reduction and packaging could support progress toward portable MCG and MEG systems, accelerating the adoption of biomagnetic imaging.

Author Contributions: Conceptualization, N.Z., A.M.P., B.L.G. and T.C.; methodology, N.Z., A.M.P., B.L.G. and T.C.; software, N.Z. and T.C.; validation, N.Z.; formal analysis, N.Z.; investigation, N.Z.; resources, T.C.; data curation, N.Z. and T.C.; writing—original draft preparation, N.Z.; writing—review and editing, A.M.P., B.L.G. and T.C.; visualization, N.Z. and T.C.; supervision, A.M.P., B.L.G. and T.C.; project administration, A.M.P., B.L.G. and T.C.; funding acquisition, T.C. All authors have read and agreed to the published version of the manuscript.

Funding: This research was funded by NSERC, grant number RGPIN-2023-05837.

Institutional Review Board Statement: The study was conducted in accordance with the Declaration of Helsinki and approved by the Ethics Committee of Simon Fraser University (protocol code 30002498 and date of approval 23 September 2025).

Informed Consent Statement: Informed consent was obtained from the subject involved in the study. Written informed consent has been obtained from the subject to publish this paper.

Data Availability Statement: The data presented in this study are available upon request from the corresponding author due to ethical restrictions (research ethics board approval) and participant privacy requirements.

Acknowledgments: During the preparation of this manuscript, the authors used ChatGPT (OpenAI; GPT-5.2) to assist with language editing for grammar and clarity. ChatGPT was also used to assist with MATLAB scripting and debugging (e.g., plotting/visualization and implementation of filtering/epoching routines). The authors reviewed and edited the output, validated the code and analyses, and take full responsibility for the content of this publication.

Conflicts of Interest: Author T.C. (Teresa Cheung) has a financial relationship to FieldLine Medical (Boulder, CO, USA). The remaining authors declare no conflicts of interest. The funders had no role in the design of the study; in the collection, analyses, or interpretation of data; in the writing of the manuscript; or in the decision to publish the results.

Abbreviations

The following abbreviations are used in this manuscript:

OPM	Optically pumped magnetometer
SQUID	Superconducting quantum interference device
MEG	Magnetoencephalography
MCG	Magnetocardiography
PPG	Photoplethysmograph

References

1. Hricak, H.; Abdel-Wahab, M.; Atun, R.; Lette, M.M.; Paez, D.; Brink, J.A.; Donoso-Bach, L.; Frija, G.; Hierath, M.; Holmberg, O.; et al. Medical Imaging and Nuclear Medicine: A Lancet Oncology Commission. *Lancet Oncol.* **2021**, *22*, e136–e172. [CrossRef] [PubMed]
2. Baillet, S. Magnetoencephalography for Brain Electrophysiology and Imaging. *Nat. Neurosci.* **2017**, *20*, 327–339. [CrossRef] [PubMed]
3. Li, J.; Shen, Y.; Shen, C.; Ning, X.; Xiang, M. Advances of Magnetocardiography in Application of Adult and Fetal Cardiac Diseases. *Front. Cardiovasc. Med.* **2025**, *12*, 1522467. [CrossRef] [PubMed]
4. Vrba, J. Magnetoencephalography: The Art of Finding a Needle in a Haystack. *Phys. C Supercond.* **2002**, *368*, 1–9. [CrossRef]
5. Vrba, J.; Robinson, S.E. SQUID Sensor Array Configurations for Magnetoencephalography Applications. *Supercond. Sci. Technol.* **2002**, *15*, R51–R89. [CrossRef]
6. Boto, E.; Holmes, N.; Leggett, J.; Roberts, G.; Shah, V.; Meyer, S.S.; Muñoz, L.D.; Mullinger, K.J.; Tierney, T.M.; Bestmann, S.; et al. Moving Magnetoencephalography towards Real-World Applications with a Wearable System. *Nature* **2018**, *555*, 657–661. [CrossRef]
7. Allred, J.C.; Lyman, R.N.; Kornack, T.W.; Romalis, M.V. High-Sensitivity Atomic Magnetometer Unaffected by Spin-Exchange Relaxation. *Phys. Rev. Lett.* **2002**, *89*, 130801. [CrossRef]
8. Xiang, J.; Yu, X.; Bonnette, S.; Anand, M.; Riehm, C.D.; Schlink, B.; Diekfuss, J.A.; Myer, G.D.; Jiang, Y. Improved Biomagnetic Signal-To-Noise Ratio and Source Localization Using Optically Pumped Magnetometers with Synthetic Gradiometers. *Brain Sci.* **2023**, *13*, 663. [CrossRef]
9. Brookes, M.J.; Leggett, J.; Rea, M.; Hill, R.M.; Holmes, N.; Boto, E.; Bowtell, R. Magnetoencephalography with Optically Pumped Magnetometers (OPM-MEG): The next Generation of Functional Neuroimaging. *Trends Neurosci.* **2022**, *45*, 621–634. [CrossRef]
10. Alem, O.; Hughes, K.J.; Buard, I.; Cheung, T.P.; Maydew, T.; Griesshammer, A.; Holloway, K.; Park, A.; Lechuga, V.; Coolidge, C.; et al. An Integrated Full-Head OPM-MEG System Based on 128 Zero-Field Sensors. *Front. Neurosci.* **2023**, *17*, 1190310. [CrossRef] [PubMed]
11. Dang, H.B.; Maloof, A.C.; Romalis, M.V. Ultrahigh Sensitivity Magnetic Field and Magnetization Measurements with an Atomic Magnetometer. *Appl. Phys. Lett.* **2010**, *97*, 151110. [CrossRef]
12. Escalona-Vargas, D.; Ramirez, A.; Siegel, E.R.; Bolin, E.H.; Eswaran, H. A Customized Bed Based Stand Alone Array of Optically Pumped Magnetometers for Fetal Magnetocardiography Measurements. *Sci. Rep.* **2025**, *15*, 7236. [CrossRef]
13. Batie, M.; Bitant, S.; Strasburger, J.F.; Shah, V.; Alem, O.; Wakai, R.T. Detection of Fetal Arrhythmia Using Optically-Pumped Magnetometers. *JACC Clin. Electrophysiol.* **2018**, *4*, 284–287. [CrossRef]
14. Limes, M.E.; Foley, E.L.; Kornack, T.W.; Caliga, S.; McBride, S.; Braun, A.; Lee, W.; Lucivero, V.G.; Romalis, M.V. Portable Magnetometry for Detection of Biomagnetism in Ambient Environments. *Phys. Rev. Appl.* **2020**, *14*, 011002. [CrossRef]
15. Jimenez-Martinez, R.; Griffith, W.C.; Wang, Y.-J.; Knappe, S.; Kitching, J.; Smith, K.; Prouty, M.D. Sensitivity Comparison of Mx and Frequency-Modulated Bell–Bloom Cs Magnetometers in a Microfabricated Cell. *IEEE Trans. Instrum. Meas.* **2010**, *59*, 372–378. [CrossRef]
16. Kominis, I.K.; Kornack, T.W.; Allred, J.C.; Romalis, M.V. A Subfemtotesla Multichannel Atomic Magnetometer. *Nature* **2003**, *422*, 596–599. [CrossRef] [PubMed]
17. Yu, Q.-Q.; Liu, S.-Q.; Wang, X.-K.; Sheng, D. Partial Measurements of the Total Field Gradient and the Field-Gradient Tensor Using an Atomic Magnetic Gradiometer. *Phys. Rev. A* **2023**, *107*, 043110. [CrossRef]
18. Zhang, R.; Mhaskar, R.; Smith, K.; Prouty, M. Portable Intrinsic Gradiometer for Ultra-Sensitive Detection of Magnetic Gradient in Unshielded Environment. *Appl. Phys. Lett.* **2020**, *116*, 143501. [CrossRef]
19. Campbell, K.; Wang, Y.-J.; Savukov, I.; Schwindt, P.; Jau, Y.-Y.; Shah, V. Intrinsic Pulsed Magnetic Gradiometer in Earth's Field. *arXiv* **2021**, arXiv:2111.12310.
20. Cooper, R.J.; Prescott, D.W.; Sauer, K.L.; Dural, N.; Romalis, M.V. Intrinsic Radio-Frequency Gradiometer. *Phys. Rev. A* **2022**, *106*, 053113. [CrossRef]

21. Oelsner, G.; IJsselsteijn, R.; Scholtes, T.; Krüger, A.; Schultze, V.; Seyffert, G.; Werner, G.; Jäger, M.; Chwala, A.; Stolz, R. Integrated Optically Pumped Magnetometer for Measurements within Earth's Magnetic Field. *Phys. Rev. Appl.* **2022**, *17*, 024034. [CrossRef]
22. Kligfield, P.; Gettes, L.S.; Bailey, J.J.; Childers, R.; Deal, B.J.; Hancock, E.W.; Van Herpen, G.; Kors, J.A.; Macfarlane, P.; Mirvis, D.M.; et al. Recommendations for the Standardization and Interpretation of the Electrocardiogram: Part I: The Electrocardiogram and Its Technology: A Scientific Statement From the American Heart Association Electrocardiography and Arrhythmias Committee, Council on Clinical Cardiology; the American College of Cardiology Foundation; and the Heart Rhythm Society Endorsed by the International Society for Computerized Electrocardiology. *Circulation* **2007**, *115*, 1306–1324. [CrossRef] [PubMed]
23. Iivanainen, J.; Borna, A.; Zetter, R.; Carter, T.R.; Stephen, J.M.; McKay, J.; Parkkonen, L.; Taulu, S.; Schwindt, P.D.D. Calibration and Localization of Optically Pumped Magnetometers Using Electromagnetic Coils. *Sensors* **2022**, *22*, 3059. [CrossRef]
24. Wyllie, R.; Kauer, M.; Wakai, R.T.; Walker, T.G. Optical Magnetometer Array for Fetal Magnetocardiography. *Opt. Lett.* **2012**, *37*, 2247. [CrossRef]
25. Sheng, D.; Perry, A.R.; Krzyzewski, S.P.; Geller, S.; Kitching, J.; Knappe, S. A Microfabricated Optically-Pumped Magnetic Gradiometer. *Appl. Phys. Lett.* **2017**, *110*, 031106. [CrossRef]
26. Lucivero, V.G.; Lee, W.; Dural, N.; Romalis, M.V. Femtotesla Direct Magnetic Gradiometer Using a Single Multipass Cell. *Phys. Rev. Appl.* **2021**, *15*, 014004. [CrossRef]
27. Finnegan, E.; Davidson, S.; Harford, M.; Jorge, J.; Watkinson, P.; Young, D.; Tarassenko, L.; Villarroel, M. Pulse Arrival Time as a Surrogate of Blood Pressure. *Sci. Rep.* **2021**, *11*, 22767. [CrossRef]
28. Surawicz, B.; Childers, R.; Deal, B.J.; Gettes, L.S. AHA/ACCF/HRS Recommendations for the Standardization and Interpretation of the Electrocardiogram: Part III: Intraventricular Conduction Disturbances: A Scientific Statement From the American Heart Association Electrocardiography and Arrhythmias Committee, Council on Clinical Cardiology; the American College of Cardiology Foundation; and the Heart Rhythm Society: Endorsed by the International Society for Computerized Electrocardiology. *Circulation* **2009**, *119*, e235–e240. [CrossRef]